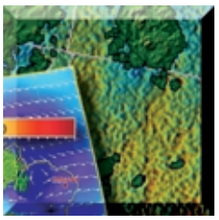

Computation of Wind Vectors over the Ocean Using Spaceborne Synthetic Aperture Radar

Jochen Horstmann, Susanne Lehner, Wolfgang Koch, and Rasmus Tonboe

The high resolution and large coverage of satellite synthetic aperture radar (SAR) offer a unique opportunity to derive mesoscale wind fields over the ocean surface and to investigate their spatial variation. For this purpose, different algorithms were developed and tested using SAR images from two European Remote Sensing satellites. In this article, the methods for deriving wind fields from SAR data are introduced. The wind directions are extracted from wind-induced streaks visible on most SAR images. Wind speeds are derived from the normalized radar cross section by applying an empirical C-band model. The different sources of error in wind retrieval that must be considered are discussed with respect to Radarsat/ScanSAR data. Furthermore, SAR-retrieved ocean surface winds are used to investigate the spatial variation of winds at different scales. (Keywords: Marine atmospheric boundary layer, Remote sensing, Synthetic aperture radar, Wind measurement, Wind variability.)

INTRODUCTION

Wind fields covering large areas are computed by meteorological models and from satellite-based wind scatterometers with a resolution of the order of 50 km. However, to study processes in the lower atmospheric boundary layer and to better understand coastal processes (e.g., currents, waves, wind, their interaction and related transport processes), a much finer spatial resolution is needed. Owing to high costs, conventional ground truth measurements can provide highly resolved wind fields only for small areas and short time periods.

The all-weather capability together with the large spatial coverage and high resolution of spaceborne synthetic aperture radars (SARs) like those aboard the European Remote Sensing satellites (ERS-1 and ERS-2) and the Canadian Radarsat offer a unique opportunity to extract ocean surface wind fields. The SARs aboard ERS-1 and ERS-2 have a spatial resolution of ≈25 m and a coverage of 100 × 100 km. The ScanSAR aboard Radarsat gives a resolution of ≈100 m with a coverage of up to 500 × 500 km. The ERS-1 and -2 SARs operate at 5.3 GHz (C band) with linear vertical (VV) polarization in transmitting and receiving at incidence angles between 20 and 26°. Radarsat ScanSAR uses the same wavelength with linear horizontal (HH) polarization in transmitting and receiving at moderate incidence angles between 20 and 50°. For the radar wavelength and the range of incidence angles of

both sensors, Bragg scattering is the main backscattering mechanism.[1–3]

The radar backscatter of the ocean surface is primarily dominated by short surface gravity waves that are in resonance with the incident radiation of the radar. The resonant water wavenumber k_w is related to the electromagnetic wavenumber k_{el} according to

$$k_w = 2k_{el} \sin \theta \ , \qquad (1)$$

where θ is the incidence angle of the radar beam. For ERS SAR, the wavelengths of scattering waves extend from 8.2 cm in the near range to 6.5 cm in the far range. These short waves are strongly influenced by the local wind field[4] and therefore allow the radar backscatter to be a measure of wind.

Much effort has been invested in the derivation of wind speed from SAR images.[5–9] The retrieval of wind direction in addition to wind speed has been investigated as well,[10–12] and the use of ScanSAR images for wind speed retrieval has also been studied.[13]

One objective of this article is to investigate the application of ERS SAR wind retrieval algorithms to Radarsat ScanSAR images. For this purpose, differences in polarization, spatial resolution, and calibration accuracy must be taken into account. The difference in spatial resolution causes increasing errors in wind speed due to a multiplicative noise in SAR images known as speckle. The error in wind speed is strongly dependent on the accuracy of the normalized radar cross section (NRCS).

A further objective is to apply the SAR-derived wind fields to investigate the spatial distribution and flux of kinetic energy in the lower atmospheric boundary layer within a range of 2 to 100 km. In contrast to SAR wind measurements, which give a snapshot of ocean surface wind fields, conventional methods collect a time series of point measurements under the assumption of Taylor's hypothesis.[14,15] Taylor assumes the turbulence to be frozen as it advects past the sensor, and thus the wind speed can be used to translate turbulence measurements as a function of time to their corresponding measurements in space. A first attempt to determine kinetic energy spectra from satellite measurements was performed by Freilich and Chelton[16] by analyzing 15 days of Seasat scatterometer winds. Their results agree well to the power law of $k^{-2.1}$ retrieved by Bauer[17] using 1 year of ERS-1 scatterometer winds at scales ranging from ≈100 to 10,000 km. The exponent -2.1 lies between the power law k^{-3} as predicted by the theory of quasi-geostrophic turbulence[18] and by the theory of two-dimensional isotropic turbulence[19] with $k^{-5/3}$. Several conventional studies have been carried out that show a spectral gap in the mesoscale range.[20]

In this article we introduce the algorithms used to derive wind fields from ERS SAR images. For validation of the algorithms, an ERS/SAR-retrieved wind field on the German coast of the Baltic Sea is compared with a mesoscale atmospheric model. Next, wind retrieval algorithms are applied to Radarsat ScanSAR images. A case study using a ScanSAR scene acquired over the southern tip of Greenland is presented. Sources of error in wind derivation from ERS SAR are described and estimated using the Radarsat ScanSAR images. Finally, ERS/SAR-derived wind fields are applied to investigate the spatial distribution and flux of the kinetic energy on scales of 2 to 100 km.

WIND FIELD RETRIEVAL

From ERS SAR Images

The ERS-1 and -2 satellites fly in a near-circular Sun-synchronous orbit at altitudes between 782 to 785 km with a 35-day repeat cycle. They have a spatial resolution between 6 and 30 m in azimuth (in-flight direction) and 26 m in range (antenna look direction). The radiometric accuracy of the SARs of both satellites is ≈0.5 dB.[21]

For derivation of wind speeds from ERS SAR images, two independent algorithms have been developed. The first one is based on the NRCS, which is strongly dependent on the small-scale roughness of the ocean surface, which in turn is strongly dependent on the local wind speed. The other algorithm is dependent on the pixel smearing in-flight direction caused by the movement of scattering facets on the ocean surface in slant range.

Empirical C-band models CMOD4[22] and CMOD-IFR2[23] are used for retrieving wind speed from the NRCS. Both models were originally developed for the ERS scatterometer, which operates at the same wavelength and moderate incidence angles between 18 and 59°. The applicability of these models to ERS SAR data is presented in detail in Ref. 9. Both models require as input the NRCS, the incidence angle of the radar beam, and the wind direction. For computation of wind speed, the NRCS must be accurately calibrated. Because of saturation of the analog-to-digital converter in case of high backscatter, the NRCS of ERS SAR images must be recalibrated as described in detail in Ref. 24.

For derivation of wind direction, the ERS SAR image is analyzed using an algorithm based on fast Fourier transforms (FFTs). This method extracts the wind directions from wind-induced streaks, which are visible in most SAR images. In ≈65% of all investigated ERS SAR images, wind streaks were found from which the wind direction could be derived. In general, this algorithm can compute the wind direction with only a 180° ambiguity. However, if shadowing of the

wind field is present, for example owing to coastal topography, the 180° ambiguity can be removed.[9,12]

The Odra Lagoon, situated on the German and Polish coast of the Baltic Sea, was chosen for a detailed analysis of SAR wind estimation techniques because of the complex structure of the wind field resulting from the topography. Since no conventional ocean surface wind measurements covering the entire region are available, the Geesthacht Mesoscale Atmospheric Simulation Model (GESIMA)[25] was used for comparison. GESIMA is a three-dimensional nonhydrostatic mesoscale model of atmospheric circulation. For the present study it was set up with eight layers between 0 and 1500 m and a horizontal resolution of 2 × 2 km. Roughness length over the water surface is given by Charnock's equation.[26] Land-use charts are used to determine roughness over land.

In Fig. 1, the ERS-1 SAR image from 18 June 1995 at 2100 UT shows the Odra Lagoon and the Pomeranian Bight of the Baltic Sea. The solid lines indicate the wind direction as computed by the FFT algorithm with a resolution of 5 × 5 km. The directional ambiguity of 180° was removed using wind shadowing effects close to the coast, which are clearly visible. The mean SAR-derived wind direction of 300° is in line with the visible streaks in Fig. 1, but does not compare well to the 10-min mean direction of 250° measured at Ueckermünde Station.

Wind speeds were computed with CMOD-IFR2 and are plotted in Fig. 2 (left) with a horizontal resolution of 2 × 2 km on the grid of the GESIMA model. The SAR-derived wind speed near Ueckermünde agrees well with ground truth measurements. Wind speeds measured at Arkona, a station 20 km northwest of Ueckermünde and representing the wind speed in the Pomeranian Bight, is slightly higher than the SAR-derived wind speeds.

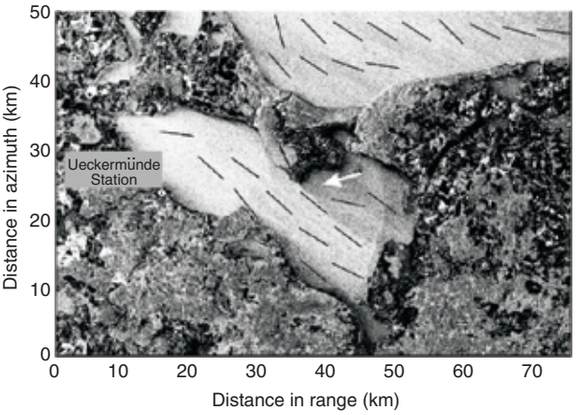

Figure 1. Image of the Odra Lagoon and the Pomeranian Bight situated on the German and Polish coasts of the Baltic Sea. The image was acquired by SAR aboard ERS-1 on 18 June 1995 at 2100 UT. Solid lines represent wind directions as computed from the imaged wind-induced streaks. The white arrow indicates wind shadowing caused by the coast.

Wind speeds computed with GESIMA are also plotted in Fig. 2 (right). They were computed as being stationary, assuming a neutral atmosphere, and taking the 10-min mean wind measurements at Ueckermünde into account. Overall, the GESIMA wind speeds agree well with the results retrieved from the ERS SAR image. The main differences occur leeward of the coast, where the model overestimates the effect of shadowing. This may be due to uncertainties in the land-use charts used by GESIMA.

From Radarsat ScanSAR Images

Radarsat was launched in November 1995 in a near-circular polar orbit at an approximate altitude of

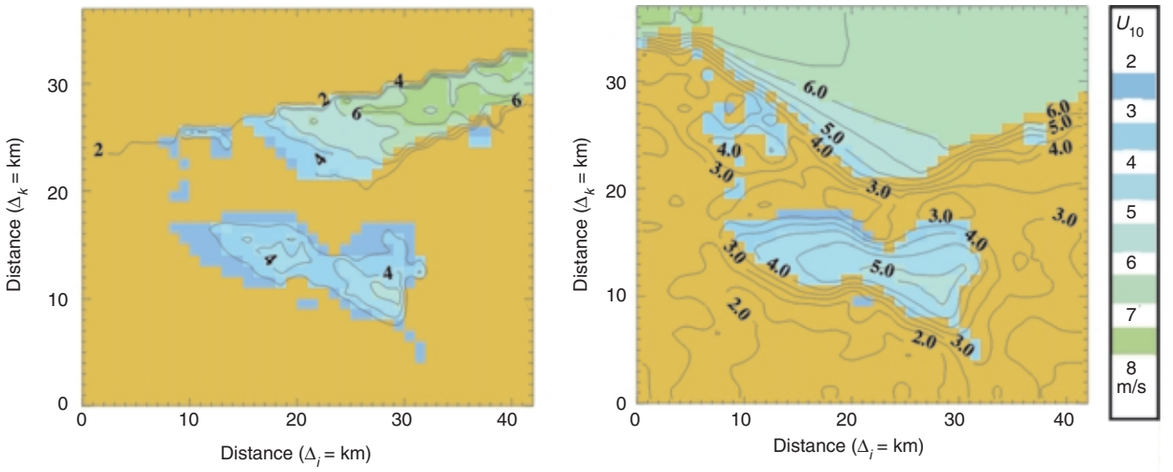

Figure 2. Wind speed plots derived from the ERS-1 SAR image shown in Fig. 1 (left) and from the Geesthacht Mesoscale Atmospheric Simulation Model (right). The color scale gives the wind speeds in 10-m height (U_{10}), and Δi and Δk are the grid cell sizes.

800 km with a repeat cycle of 24 days (about 14 orbits per day). SAR is the only instrument onboard. The images from the ScanSAR wide swath A mode have pixel sizes of 50 m and a swath width of ≈500 km. The swath of the ScanSAR wide A scene comprises four beams (w1, w2, w3, and s7) covering, sequentially, four areas in range. The resolution for the four beams differs from 86.5 to 146.8 m in range and 93.1 to 117.5 m in azimuth. The radiometric accuracy differs over the scene and can reach values of 1.6 dB.[27]

Radarsat ScanSAR wide mode is an attractive feature for ice mapping. Soon after the launch of Radarsat, the data were used for operational sea ice charting by the Canadian Ice Service.[28] The operational ice monitoring service for Greenland at the Danish Meteorological Institute has been evaluating these data[29] since 1996. Wind speed estimates from Radarsat will be used to facilitate ice drift forecasting and interpretation of the image.

For wind field retrieval from Radarsat ScanSAR wide swath, the C-band wind models CMOD4 and CMOD-IFR2 were applied. Both scatterometer algorithms were calibrated using the C-band ERS scatterometer with VV polarization. To extract wind speeds from Radarsat ScanSAR images, the differences in NRCS due to HH polarization were taken into account. The VV/HH polarization cross-sectional differences measured at moderate incidence angles and predicted by commonly used rough ocean surface scattering models (e.g., the Bragg facet model[2,30]) are significant. For example, Unal et al.[31] measured differences in NRCS of <5.5 dB between VV and HH polarization at incidence angles of 45°, winds of 10 ms^{-1} toward the antenna, and a radar frequency of 5.3 GHz; the Bragg facet model predicts differences of <9.5 dB, independent of the radar frequency. Investigations obtained with Radarsat SAR using the measurements of Unal et al. showed minimal differences in NRCS between HH and VV polarization.[32]

For the work reported in this article, an empirical expression according to Thompson et al.[13] was applied to account for HH polarization when using the C-band models. The expression has the form

$$\sigma_0^{HH} = \frac{(1+\alpha\tan^2\theta)^2}{(1+2\tan^2\theta)^2}\sigma_0^{VV}(U_{10},\theta,\phi)\,, \qquad (2)$$

where

θ = incidence angle,
U_{10} = wind speed at 10-m height,
ϕ = wind direction versus antenna look direction,
σ_0^{VV} = NRCS from the C-band model,
σ_0^{HH} = resulting NRCS for HH polarization, and
α = constant equal to 0.6.

In Fig. 3, the NRCS are plotted versus wind directions for wind speeds between 5 and 25 ms^{-1} for HH (solid curves) and VV polarization (dotted curves) at a 45° incidence angle. The NRCS were computed using CMOD-IFR2 for VV polarization and considering the HH polarization given in Eq. 2. According to Fig. 3, the difference in NRCS between HH and VV polarization for wind directed toward the antenna (upwind) and a wind speed of 10 ms^{-1} is ≈5.5 dB, which agrees well with the measurements of Unal et al.[31]

For the derivation of wind speeds with the C-band models, the NRCS from Radarsat ScanSAR wide swath images had to be derived. This was done according to Shepherd.[33] The accuracy of the NRCS from these images changes depending on the incidence angle of the radar beam, as noted earlier, and the calibration of the different processing facilities. Problems occur especially at the beam overlap. Figure 4 shows the NRCS of such an image of Cape Farewell, the southern part of Greenland (59 to 61°N, 38 to 48°W), acquired on 25 February 1999 at 20:39 UT. The typical decrease of the NRCS with increasing incidence angle over the ocean surface, due to Bragg scattering, is seen in range. Furthermore, vertical stripes in the azimuth direction are detected, e.g., at ranges of 190, 390, and 430 km. These stripes were observed in all investigated Radarsat ScanSAR wide images and are attributed to the insufficient calibration of the data.

Sea ice is also imaged along the east coast of Greenland as several wind-induced stripes, especially along the southwest coast (Julianehaab Bay). On the east side of Cape Farewell and in the Julianehaab Bay, the strong influence of topography on the wind field is seen. Figure 5 shows the wind speeds as computed with CMOD-IFR2 and Eq. 2, assuming a fixed wind direction of

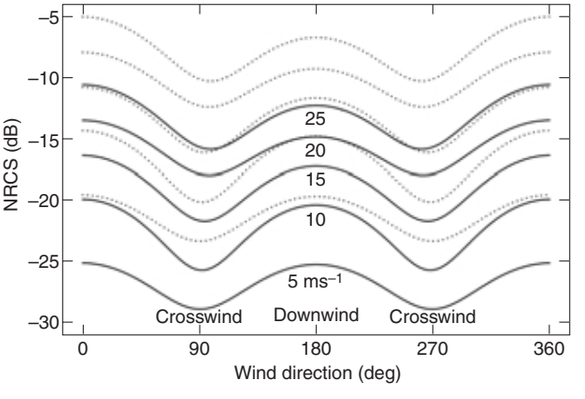

Figure 3. NRCS are plotted versus wind directions for HH polarization (solid curves) and VV polarization (dotted curves) for wind speed between 5 and 25 ms^{-1}. These cross sections were computed for a fixed incidence angle of 45° using the C-band model CMOD-IFR2 for VV polarization and considering the empirical relation given in Eq. 2 for HH polarization.

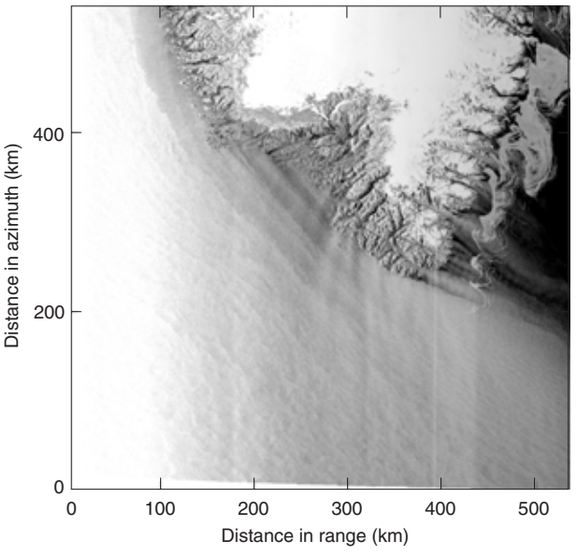

Figure 4. This gray scale gives the NRCS of the Radarsat ScanSAR wide swath image of the Cape Farewell area of Greenland. The image covers approximately the area between 59 to 61°N, 38 to 48°W, and was acquired on 25 February 1999 at 2039 UT. (© Danish Meteorologic Institute and Radarsat International.)

310°. The wind speeds are given in a gray scale between 0 and 30 ms^{-1}. Superimposed are the isotaches in steps of 2.5 ms^{-1}. The wind direction of 310° agrees well with the direction of streaks visible in Fig. 4. A ship near 550 km in range and 190 km in azimuth, a few kilometers east of the imaged area, reported wind speeds of 12 ms^{-1} and a wind direction of 300°. The increase of wind speeds with range across the whole image does not agree with the weather charts and was an effect observed in most investigated images, especially in the presence of high wind speeds. This effect is probably due to insufficient calibration of the sensor, which is not yet accurate enough for wind speed retrieval using SAR. Another source of error could be the VV/HH polarization cross-section ratio, which is not well known in the entire range of ScanSAR. For Radarsat ScanSAR images acquired under low wind speed conditions (≈10 ms^{-1}), CMOD-IFR2–retrieved wind fields showed no distinct range dependency, but produced excessive overall wind speeds.

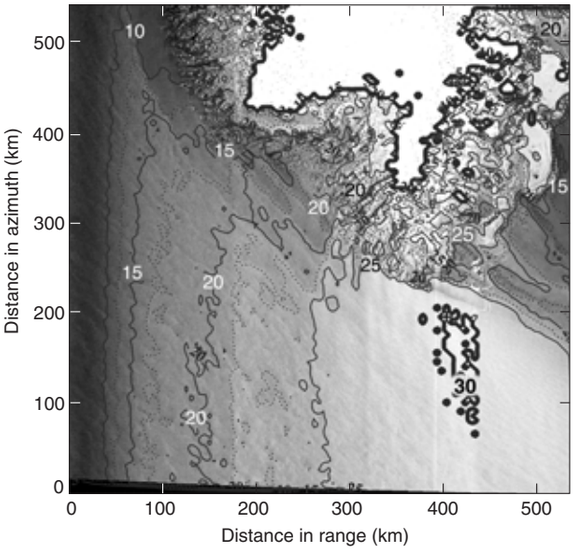

Figure 5. Wind speeds were computed using CMOD-IFR2 with a fixed wind direction of 310°. Gray scale values from black to white give the wind speeds between 0 and 30 ms^{-1}. Superimposed are the isotaches in steps of 2.5 ms^{-1}. (© Danish Meteorologic Institute and Radarsat International.)

ERROR SOURCES IN SAR WIND SPEED RETRIEVAL

When retrieving wind speeds from SAR images with C-band models, sources of error are present that affect the accuracy of measurement. Most errors are caused by the effect of grid cell size, uncertainty in wind direction, and the reliability of the NRCS. Figure 6 demonstrates the effect of grid cell size on SAR-derived wind speeds. To see this effect, a SAR image acquired under homogeneous wind conditions is needed. For this purpose, the ERS-1 SAR image of the North Sea from 1 December 1995 was chosen, supported by weather charts together with time series measured from the R/V *Gauss*. Wind speeds were computed using the CMOD4, a mean SAR-derived wind direction of 175°, and a mean NRCS from grid cell sizes between 0.1 and 40 km. The mean wind speed, ≈15 ms^{-1}, agrees well with the 10-min mean ground truth measurements of 167° and 15.3 ms^{-1} from the *Gauss*. In Fig. 6, the resulting wind

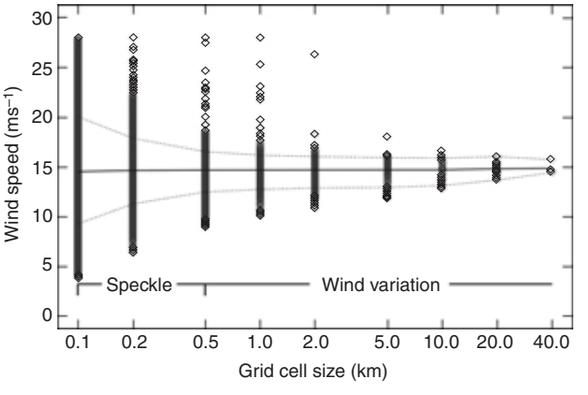

Figure 6. The effect of grid cell size on wind speed measurements is plotted for ERS SAR. Each diamond represents the mean wind speed of a grid cell. The solid curve represents the mean wind speed of the whole image, and the dashed curves give the 90% confidence interval.

speed values are plotted versus the corresponding grid cell sizes. The 90% confidence interval is indicated by the dashed curves. The scatter of wind speed between 0.1 and 0.5 km is mainly influenced by the effect of speckle[34] and small-scale changes in wind direction. For resolutions above 0.5 km, wind variability dominates the scatter.

The major source of wind speed error results from the need for information on wind direction as input into the C-band models. In Fig. 7, the relative error in wind speed is plotted, assuming an uncertainty in wind direction of ±10°. The computations were performed with the CMOD4 for VV polarization and a constant incidence angle of 23°. Wind speeds were varied from 3 to 25 ms^{-1} and wind directions between 90° (upwind) and 270° (downwind) clockwise to the flight direction. The largest errors result from wind directions of 135 and 225°, respectively (Fig. 7), and at 45 and 315°, owing to the symmetry of C-band models. The increase of error due to increasing incidence angles is negligible for the range of ERS SAR images. For Radarsat ScanSAR, the error in wind speed decreases with incidence angles owing to the decrease of the upwind crosswind ratio with incidence angles.

In addition, the error in wind speed is dependent on the accuracy of the NRCS of each SAR. The NRCS measured by both ERS-1 and -2 SAR is normally in the range of ±0.5 dB.[21,24] For inhomogeneous images with very high backscatter, ≈0 dB, the error can increase depending on the calibration procedure.[9] The radiometric accuracy of Radarsat ScanSAR is dependent on the processing facility and is up to 1.6 dB.[27] These inaccuracies of NRCS lead to large errors in wind speed, especially in the case of high wind speeds and small incidence angles.

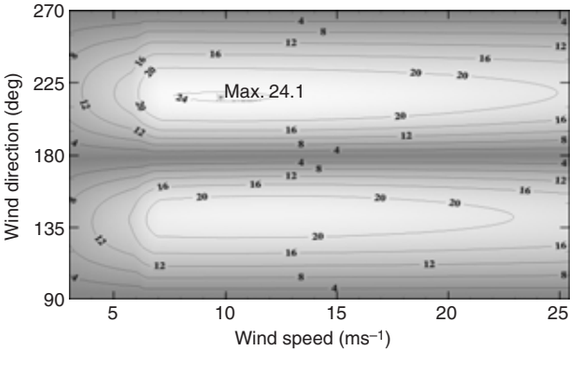

Figure 7. Estimated relative error in percentage of wind speed due to an uncertainty in wind direction of ±10° for an incidence angle of 23°. The error was computed for wind speeds from 3 to 25 ms^{-1} and wind directions between 90° (upwind) and 270° (downwind). The wind direction is given clockwise from the radar look direction, e.g., 90° corresponds to upwind, 180° to crosswind, and 270° to downwind.

WIND VARIABILITY

Again, the high accuracy and the large area coverage of ERS/SAR-derived wind fields yield a unique opportunity to investigate spatial variations of surface wind fields. In Fig. 8, the ERS-1 SAR image of a 100 × 100 km area northwest of the Shetland Islands is shown. The image was acquired on 1 December 1992 at wind speeds of ≈14 ms^{-1}. A range traveling wave system with wavelengths of ≈300 m was imaged by the SAR over the whole region. The superimposed solid lines in the highlighted area of Fig. 8 represent the wind directions, which were computed from the wind streaks visible in the image. Because of wind shadowing from the coasts of the islands, the directional ambiguity of 180° could be removed. Taking the mean wind direction as input for the CMOD-IFR2, the wind speeds were computed for a grid cell size of 100 × 100 m. The resulting mean wind speed of the highlighted area was 14.1 ms^{-1}.

To investigate the spectral distribution of the wind, wind speeds were transformed with a two-dimensional FFT into the wavenumber domain. Figure 9 shows the resulting energy spectrum with range and azimuth wavenumbers plotted on the *x* and *y* axes, respectively. The axes on the right and top give the corresponding wavelengths. The intensity of the spectral amplitude was weighted to highlight the effects visible in the spectrum. The areas containing the highest spectral power are encircled. The peaks at wavenumbers −0.02 and 0.02 rad/m in range are due to the sea state and are not of interest in this study. The area indicated by the ellipsoid shows the effect of the wind-induced streaks visible in Fig. 8, from which the wind directions were extracted. The spectral amplitude seems to increase with decreasing absolute wavenumbers below 0.003 rad/m, corresponding to wavelengths of ≈2 km.

To obtain an estimate for the decrease of spectral amplitude with increasing wavenumber, the wind speed

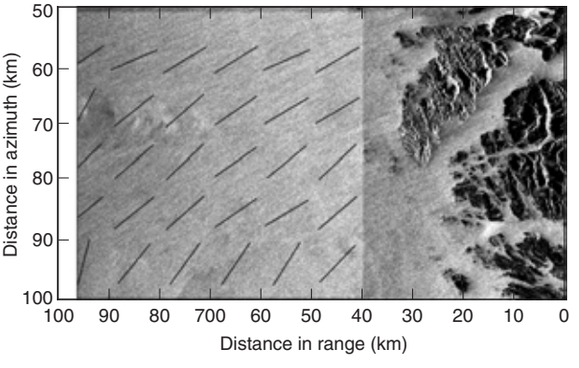

Figure 8. ERS-1 SAR image off the northwest coast of the Shetland Islands from 1 December 1992. The superimposed solid lines in the highlighted area give the derived wind direction.

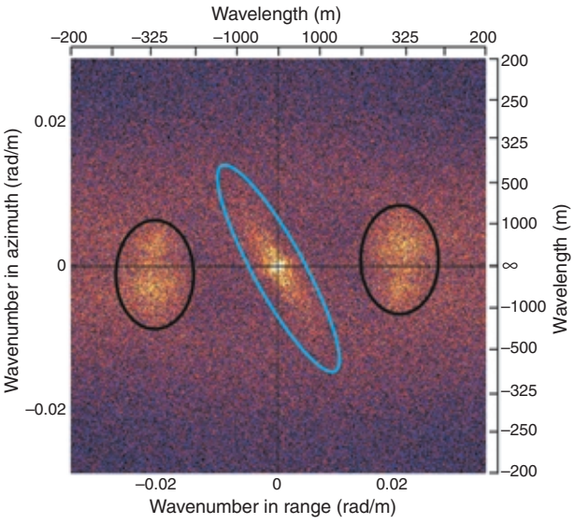

Figure 9. Energy spectrum of wind speeds retrieved from the highlighted area in Fig. 8. The black encircled areas show the peaks due to sea state, and the ellipsoid points out the energy increase caused by the effect of wind streaks.

spectrum was integrated over all directions and plotted in log–log coordinates (Fig. 10). The wavenumber and corresponding wavelength are plotted versus the spectral energy density of the wind speed. Between ≈56 and 2 km, the spectral energy density decreases, while for lower wavelengths it begins to increase. This tendency was observed on all investigated ERS/SAR-retrieved wind fields. The slope of the spectra between 100 and 2 km varied between −1.1 and −1.6, which is close to the exponent of −5/3 predicted by two-dimensional isotropic turbulence. The slope below wavelengths of

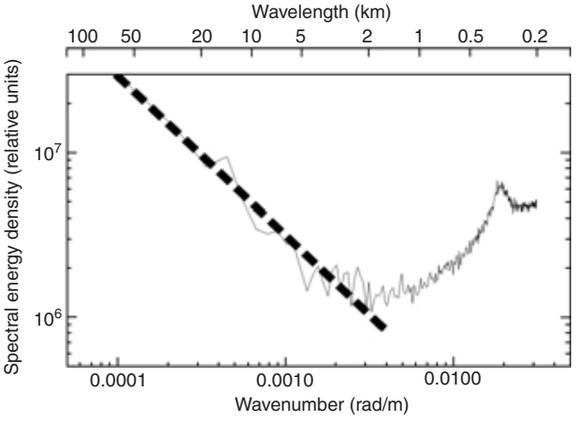

Figure 10. Wavenumber versus spectral energy density and the regression line for wavelengths down to 2 km are plotted in log–log coordinates. The spectral energy density was computed from the wind speed energy spectrum in Fig. 9. The corresponding wavelengths are also shown (slope = −1.11).

2 km is approximately 1, which is strongly influenced by speckle. The strong changes of the spectral energy density in Fig. 10 at wavelengths of ≈300 m are due to the image ocean waves. A decrease in spectral energy density with wavelengths in the boundary layer is a commonly observed phenomenon.[16,17,35] Because of the distribution of speckle for grid cell sizes smaller than 2 × 2 km, the effect of speckle begins to dominate over the wind variation, and the spectral energy density starts to increase.

CONCLUSION

Algorithms for wind field retrieval using SAR data were presented and tested on ERS-1 and -2 SAR images. Wind speeds were computed by an algorithm based on the C-band models CMOD4 and CMOD-IFR2, which were originally developed for the ERS scatterometer. Coastal mesoscale wind fields computed from ERS SAR compared well to the results of the GESIMA model. SAR-retrieved wind fields showed a finer detail in wind variations, resulting in valuable additional information. Wind directions were extracted from wind-induced stripes visible in most SAR images using an FFT-based algorithm. In ≈65% of the investigated ERS-1 and -2 SAR images, wind directions could be retrieved with a directional ambiguity of 180°. If wind shadowing was visible in the SAR images, this ambiguity could be removed.

Because of the very low spatial resolution, wind directions could not be retrieved with sufficient accuracy from Radarsat ScanSAR wide swath images, although wind streaks were clearly visible. Using C-band models with an additional empirical term to account for VV/HH ratios, wind speeds were retrieved from Radarsat ScanSAR images. For most of the investigated images, an overestimation of wind speed was found. For high wind speed situations, a range dependence of wind speed was observed. The major error can be explained by the insufficient accuracy in calibration of the NRCS for wind speed retrieval using C-band models. Another source of error can be due to the VV/HH polarization cross-section ratio, which is not well known over the whole range of ScanSAR images.

When retrieving wind speeds from SAR images with the C-band models, the main errors are caused by the effect of grid cell size, uncertainty in wind direction, and the reliability of the NRCS. For grid cell sizes below 2 km, speckle begins to dominate the retrieved wind variation, although grid cell sizes over 500 m should be chosen when using ERS SAR images. The highest errors due to uncertainties in wind directions occur especially for wind directions of 45, 135, 225, and 315° versus an antenna look direction. With increasing incidence angles and wind speed, the errors increase. This error source is independent of the

sensor's polarization, assuming the VV/HH polarization ratio is used.

Studies of spatial wind variation over the ocean surface with ERS-1 and -2 SAR showed a distinct reduction of spectral energy density with increasing wavenumber in the range of 2 to 100 km. The decrease of spectral energy density is similar to the power law $k^{-5/3}$ predicted by the theory of two-dimensional isotropic turbulence. In the range below 2 km, speckle and small-scale phenomena, e.g., sea state, start to compensate for the effect of wind variation.

REFERENCES

[1]Wright, J. W., "Backscattering from Capillary Waves with Application to Sea Clutter," *IEEE Trans. Antennas Propag.* **AP-14**(6), 749–754 (Nov 1966).

[2]Valenzuela, G. R., "Theories for Interaction of Electromagnetic and Oceanic Waves—A Review," *Boundary Layer Meteorol.* **13**, 61–85 (1978).

[3]Wetzel, L. B., "Sea Clutter," Chap. 13, in *Radar Handbook*, 2nd Ed., M. I. Skolnik (ed.), McGraw-Hill, New York, pp. 13.1–13.36 (1990).

[4]Phillips, O. M., "Spectral and Statistical Properties of the Equilibrium Range in Wind-Generated Gravity Waves," *J. Fluid Mech.* **156**, 505–531 (1985).

[5]Alpers, W. R., and Brümmer, B., "Atmospheric Boundary Layer Rolls Observed by the Synthetic Aperture Radar Aboard the ERS-1 Satellite," *J. Geophys. Res.* **99**, 12,613–12,621 (1994).

[6]Chapron, B., Elfouhaily, T., and Kerbaol, V., "A SAR Speckle Wind Algorithm," in *Proc. Second ERS-1 Workshop*, Inst. Fr. de Rech. pour l`Exploit. de la Mer, Brest, France, pp. 5–40 (1994).

[7]Rosenthal, W., Lehner, S., Horstmann, J., and Koch, W., "Wind Measurements Using ERS-1 SAR," in *Proc. Second ERS Applications Workshop*, ESA SP-383, pp. 355–358 (Dec 1995).

[8]Scoon, A., Robinson, I. S., and Meadows, P. J., "Demonstration of an Improved Calibration Scheme for ERS-1 SAR Imagery Using a Scatterometer Wind Model," *Int. J. Remote Sens.* **17**(2), 413–418 (1996).

[9]Horstmann, J., *Investigation of Wind Speed Retrieval with Synthetic Aperture Radar Aboard the ERS-1/2 Satellites*, GKSS 97/E/55 (1997).

[10]Wakerman, C. C., Rufenach, C. L., Schuchman, R., Johannessen, J. A., and Davidson, K., "Wind Vector Retrieval Using ERS-1 Synthetic Aperture Radar Imagery," *J. Geophys. Res.* **34**, 1343–1352 (1996).

[11]Vachon, P. W., and Dobson, F. W., "Validation of Wind Vector Retrieval from ERS-1 SAR Images over the Ocean," *Global Atm. Ocean Syst.* **5**, 177–187 (1996).

[12]Lehner, S., Horstmann, J., Koch, W., and Rosenthal, W., "Mesoscale Wind Measurements Using Recalibrated ERS SAR Images," *J. Geophys. Res.* **103**, 7847–7856 (1998).

[13]Thompson, D. R., Elfouhaily, T. M., and Chapron, B., "Polarization Ratio for Microwave Backscattering from the Ocean Surface at Low to Moderate Incidence Angles," in *Proc. IGARSS '98*, Seattle, WA (1998).

[14]Taylor, G. I., "The Spectrum of Turbulence," *Proc. Roy. Soc.* **A164**, 476–490 (1938).

[15]Powell, D. C., and Elderkin, C. E., "An Investigation of the Application of Taylor's Hypothesis to Atmospheric Boundary Layer Turbulence," *J. Atmos. Sci.* **31**, 990–1002 (1974).

[16]Freilich, M. H., and Chelton, D. B., "Wavenumber Spectra of Pacific Winds Measured by the Seasat Scatterometer," *Am. Met. Soc.* **16**, 741–757 (1986).

[17]Bauer, E., "Statistical Comparison of Winds from ERS-1 Scatterometer and ECMWF Model in Time and Wavenumber Domain," in *Proc. Third ERS Symp.—Space at the Service of Our Environment*, ESTEC, Florence, Italy, pp. 1195–1200 (1997).

[18]Charney, J. G., "Geostrophic Turbulence," *J. Atmos. Sci.* **28**, 1087–1095 (1971).

[19]Kraichnan, R. H., "Inertial-Range Transfer in a Two- and Three-Dimensional Turbulence," *J. Fluid Mech.* **47**, 525–535 (1971).

[20]Van der Hoven, I., "Power Spectrum of Horizontal Wind Speed in the Frequency Range from 0.0007 to 900 Cycles per Hour," *J. Meteor.* **14**, 160 (1957).

[21]Meadows, P., Laur, H., Sanchez, J. I., and Schättler, B., "The ERS SAR Performance," in *Proc. CEOS SAR Workshop*, Noordwijk, The Netherlands, pp. 223–232 (1998).

[22]Stoffelen, A., and Anderson, D., "Scatterometer Data Interpretation: Estimation and Validation of the Transfer Function CMOD4," *J. Geophys. Res.* **102**, 5767–5780 (1997).

[23]Quilfen, Y., and Bentamy, A., "Calibration/Validation of ERS-1 Scatterometer Precision Products," in *Proc. IGARSS '94*, Pasadena, CA, pp. 945–947 (1994).

[24]Laur, H., Bally, P., Meadows, P., Sanchez, J., Schaettler, B., and Lopinto, E., *Derivation of the Backscattering Coefficient σ_0 in ESA ERS SAR PRI Products*, Tech. Note ES-TN-RS-PM-HL09, Issue 2, Rev. 4, European Space Agency, Frascati, Italy (May 1997).

[25]Kapitza, H., and Eppel, D. P., "The Non-Hydrostatic Mesoscale Model GESIMA., I, Dynamical Equations and Tests," *Contrib. Atmos. Phys.* **65**(2), 129–146 (May 1992).

[26]Charnock, H., "Wind Stress on a Water Surface," *Quart. J. Roy. Meteorol. Soc.* **81**, 639–640 (1955).

[27]Srivastava, S. K., Banik, B. T., Adamovic, M., Hawkins, R. K., Lukowski, T. I., et al., "RADARSAT Image Quality and Calibration Performance—Update," in *Proc. IGARSS '98*, Seattle, WA (1998).

[28]Ramsay, B. R., "The Use of RADARSAT Data Within the Canadian Ice Service," in *Proc. 6th Workshop of the Canadian Ice Working Group* (1996).

[29]Gill, R. S., and Valeur, H. H., *Evaluation of the Radarsat Imagery for the Operational Mapping of Sea Ice Around Greenland*, Scientific Report 96-9, Danish Meteorologic Institute, Copenhagen (1996).

[30]Wright, J. W., "A New Model for Sea Clutter," *IEEE Trans. Antennas Propagat.* **AP-16**(2), 217–223 (1968).

[31]Unal, C. M. H., Snooji, P., and Swart, P. J. F., "The Polarization-Dependent Relation Between Radar Backscatter from the Ocean Surface and Surface Wind Vectors at Frequencies Between 1 and 18 GHz," *IEEE Trans. Geosci. Remote Sens.* **29**, 621–626 (1991).

[32]Vachon, P. W., Campbell, J. W. M., Bjerkelund, C., Dobson, F. W., and Rey, M. T., "Ship Detection by the RADARSAT SAR: Validation of Detection Model Predictions," *Can. J. Remote Sens.* **23**(1), 48–59 (1997).

[33]Shepherd, N., *Extraction of Beta Nought and Sigma Nought from RADARSAT CDPF Products*, Report AS97-5001 Rev. 1, Altrix Systems, Ottawa, Ontario, Canada (1997).

[34]Bally, P., and Fellah, K., *Evaluation of the Accuracy of the Backscattering Coefficient Measurement in SAR Data Products*, Technical Note, European Space Research and Technology Center, Noordwijk, The Netherlands (Jul 1995).

[35]Kaimal, J. C., Wyngaard, J. C., Izumi, Y., and Cote, O. R., "Spectral Characteristics of Surface Layer Turbulence," *Quart. J. Roy. Meteorol. Soc.* **98**, 563–589 (1972).

ACKNOWLEDGMENTS: The authors from the GKSS Research Center and from the Deutsches Zentrum für Luft- und Raumfahrt were supported by the German Bundesministerium für Bildung und Forschung (BMBF) through SARPAK and ENVOC projects.

THE AUTHORS

JOCHEN HORSTMANN is with the GKSS Research Center, Institute of Hydrophysics, Geesthacht, Germany. His e-mail address is horstmann@gkss.de.

SUSANNE LEHNER is affiliated with Deutsches Zentrum für Luft- und Raumfahrt, D-Wessling. Her e-mail address is Susanne.Lehner@dlr.de.

WOLFGANG KOCH is with the GKSS Research Center, Geesthacht, Germany. His e-mail address is frkochw@gkss.de.

RASMUS TONBOE is with the Meteorological Institute, Copenhagen, Denmark. His e-mail address is rtt@dmi.dk.